Anisotropic Nonsaturating Magnetoresistance Observed in $HoMn_6Ge_6$: A Kagome Dirac Semimetal

Achintya Low, Tushar Kanti Bhowmik, Susanta Ghosh, and Setti Thirupathaiah*
Department of Condensed Matter Physics and Material Sciences,
S. N. Bose National Centre for Basic Sciences, Kolkata-700106

We report the magnetic and magnetotransport properties and electronic band structure of the kagome Dirac semimetal $HoMn_6Ge_6$. Temperature-dependent electrical resistivity demonstrates various magnetic-transition-driven anomalies. Notably, a crossover from negative to positive magnetoresistance (MR) is observed at around 150 K. While the linear nonsaturating positive MR in the low-temperature region is mainly driven by the linear Dirac-like band dispersions as predicted by the first-principles calculations, the negative MR observed in the high-temperature region is due to the spin-flop type magnetic transition. Consistent with anisotropic Fermi surface topology, we observe anisotropic magnetoresistance at low temperatures. A significant anomalous Hall effect has been noticed at high temperatures in addition to a switching of the dominant charge carrier from electron to hole at around 215 K.

I. INTRODUCTION

The combination of frustrated magnetism, strong electronic correlations, and quantum topology in the kogome systems immensely attracts researchers from the fundamental science and potential technological applications points of view [1–8]. Particularly, the interplay among these peculiar physical properties in the kagome lattice features intriguing quantum phenomena, including the quantum spin liquid phase [9–12], flat bands [13–16], Dirac and Weyl fermions [15, 17–21], Chern quantum phase [22, 23], and Skyrmionic lattice [24, 25]. So far, the transition metal-based kagome systems have been extensively explored to find the Weyl fermions in Mn_3Sn(Ge) [18, 26], giant anomalous Hall effect in $Co_3Sn_2S_2$ [19], Nernst effect in Fe_3Sn [27], Skyrmion lattice in Fe_3Sn_2 [28]. On the other hand, the recent discovery of a nearly ideal quantum limit Chern magnet with massive Dirac fermion in $TbMn_6Sn_6$ has ignited an intense search for rare-earth-based kagome systems [23].

Following this discovery, several experimental reports appeared discussing the tuning of topological properties in RMn_6Sn_6 (R = Gd-Tm, Lu) [29], large anomalous Hall effect in RMn_6Sn_6 (R = Tb, Dy, and Ho) [30], Chern magnetic state in $TbMn_6Sn_6$ [23], Dirac-like band crossings in $HoMn_6Sn_6$ [31], linear unsaturated magnetoresistance in RMn_6Sn_6 (R = Gd, Tm, Lu) [29]. Among these, $HoMn_6Sn_6$ is a ferrimagnetic metal in which the spins of the Ho-4f sub-lattice align antiferromagnetically with the spins of the Mn-3d sub-lattice. Thus, the interplay between the ferrimagnetism and the electronic band structure plays a vital role in shaping the linear nonsaturated magnetoresistance of this system [29, 31, 32]. On the other hand, though $HoMn_6Ge_6$ shares a similar crystal structure to $HoMn_6Sn_6$, minimal information is available on the magnetotransport properties of $HoMn_6Ge_6$ discussing in detail the relation between magnetic and magnetotransport properties [33].

$HoMn_6Ge_6$ crystallizes into $HfFe_6Ge_6$-type hexagonal structure with a space group of $P6/mmm$, ordering antiferromagnetically at a Néel temperature of 466 K [34]. The magnetic moments of Mn and Ho are arranged in a skew-spiral ($\widetilde{SS}$) fashion, and the plane of magnetic moments (Ho and Mo) is angled at 60^o with the z-axis in $HoMn_6Ge_6$ [35]. In contrast, in RMn_6Sn_6 systems, the moments of R and Mn are aligned antiparallel to form a ferrimagnetic structure with an easy-axis of magnetization angled with the z-axis [23, 29–31]. The angle between the z-axis and the easy-axis of magnetization strongly depends on the rare-earth element [23, 29–31, 35, 36]. Further, as discussed in Ref. [35], the magnetic structure of these systems is very sensitive to the sample temperature. For instance, in the low-temperature region (< 55 K), the Ho and Mn magnetic moments form a skew-spiral ($\widetilde{SS}$) structure, coupled antiferromagnetically, with a plane of moments making an angle θ_S with the z-axis, producing finite net magnetization along both the in-plane and out-of-plane directions. However, as the temperature is increased, the skew-spiral structure gets distorted, and the other magnetic transitions emerge at 220 and 260 K. Beyond 260 K, the $\widetilde{SS}$ structure completely gets destroyed, and the system enters a cycloid state beyond 300 K [35].

In this work, high-quality single crystals of $HoMn_6Ge_6$ were grown using the Sn flux to study the magnetic and magnetotransport properties. Electrical resistivity demonstrates an overall metallic nature throughout the measured temperature range with a few magnetic transition-driven anomalies. A crossover from negative to positive magnetoresistance (MR) is observed at a critical temperature of 150 K. While the Dirac-like linear band dispersion mainly drives the linear nonsaturating positive MR in the low-temperature region, the negative MR observed in the higher temperature region is due to the spin-flop type magnetic transition. Most importantly, we identify a large anisotropy in the magnetore-

* setti@bose.res.in

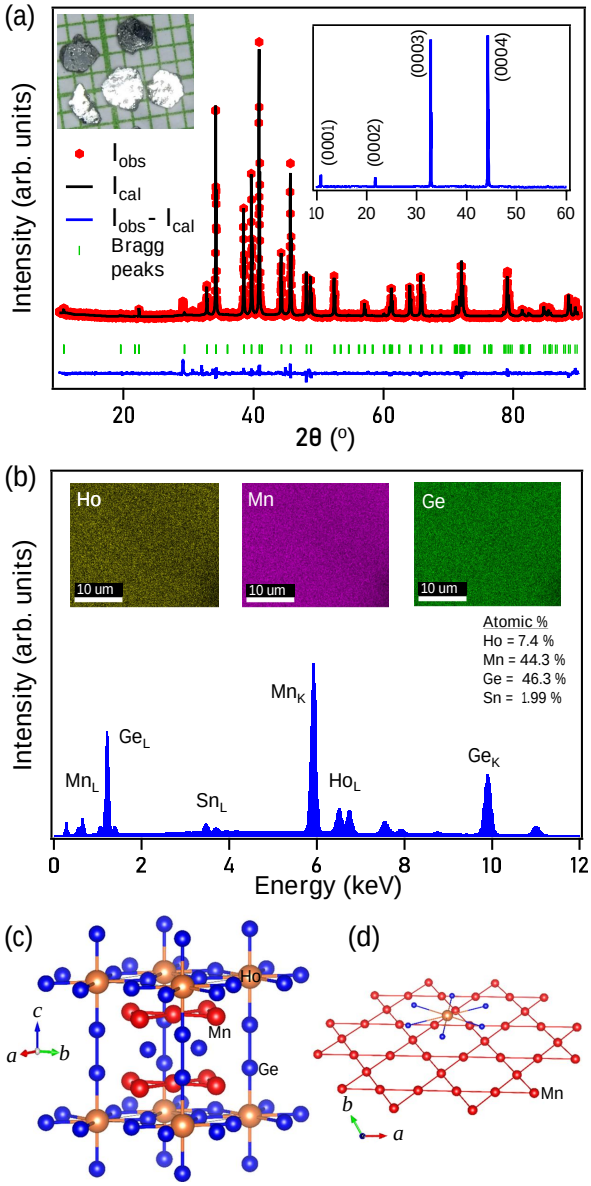

FIG. 1. (a) The powder XRD pattern taken on the crushed single crystals of $HoMn_6Ge_6$ overlapped with Rietveld refinement. The left inset in (a) shows an optical image of as-grown single crystals. The right inset in (a) represents the XRD pattern corresponding to the (000l) Bragg plane of the $HoMn_6Ge_6$ single crystal. (b) EDXS data taken on $HoMn_6Ge_6$ single crystal. Insets in (b) show the elemental mapping of Ho, Mn, and Ge atoms. (c) Schematic representation of the primitive unit cell of $HoMn_6Ge_6$. (d) Kagome lattice plane formed by the Mn atoms when projected onto the ab-plane.

sistance due to the anisotropic Fermi surface present in this system. Further, we observe anomalous Hall effect in addition to a switching of dominant charge carriers from electrons to holes at around 215 K, ingoing from high to low temperatures. Also, we performed density functional theory calculations on $HoMn_6Ge_6$ by considering the experimentally obtained skew-spiral magnetic structure to understand our magnetotransport data better [35].

II. EXPERIMENTAL AND FIRST-PRINCIPLES CALCULATION DETAILS

Single crystals of $HoMn_6Ge_6$ were grown using Sn flux. Firstly, Holmium (Ho) chunk (Alfa Aesar, 99.9%), Manganese (Mn) powder (Alfa Aesar, 99.95%), Germanium (Ge) powder (Alfa Aesar, 99.99%), and Tin (Sn) shots (Alfa Aesar, 99.995%) were weighed in the ratio of 1 : 6 : 6 : 24. The mixture was kept in an alumina crucible and sealed the crucible together with the mixture inside an evacuated quartz ampoule. The mixture was heated up to 1000^{o}C at a rate of 50^o/hr and kept there for another 18 hrs before cooling the molten mixture down to 600^{o}C at a rate of 5^{o}C/hr. Finally, the molten is annealed for another two days at 600^{o}C. Then, the ampoule was quickly transferred to a centrifuge to separate the Sn flux from the samples. In this way, we obtained several hexagonal-shaped $HoMn_6Ge_6$ single crystals with a typical size of 2mm × 2mm × 0.4mm as shown in the inset of Fig. 1(a). X-ray diffraction (XRD) was done on flat-shaped single crystals and as well on the powders of crushed crystals using Rigaku SmartLab with 9 kW Cu K_α x-ray source. The exact chemical composition of the as-grown single crystals was found using the energy dispersive x-ray spectroscopy (EDXS). The electrical resistivity and magnetotransport measurements were performed using the four-probe and Hall-probe connections. Electrical, magnetic, and magnetotransport measurements were performed in a 9 T physical properties measurement system (PPMS, DynaCool of Quantum Design) using the VSM and ETO options. To eliminate the longitudinal voltage contributions due to a possible misalignment of the Hall connections, the Hall resistivity was calculated using the relation $\frac{\rho_H(H)-\rho_H(-H)}{2}$.

To understand the magnetotransport properties, the electronic band structure of $HoMn_6Ge_6$ was calculated using the density-functional theory (DFT) within the Perdew-Burke-Ernzerhof-type generalized-gradient approximation (GGA) [37] as implemented in the Quantum Espresso (QE) simulation package [38]. The electronic wavefunction is expanded using plane waves up to a cutoff energy of 100 Ry. Brillouin zone sampling is done over a 10×10×6 Monkhorst-Pack k-grid. The crystal structure was optimized through the variable-cell relaxation method as implemented in QE. Notably, the non-collinear skew-spiral magnetic structure was considered to determine the ground state electronic properties. The band structure was produced with and without considering the spin-orbit coupling (SOC).

III. RESULTS AND DISCUSSIONS

Figure 1(a) depicts the x-ray diffraction (XRD) pattern of the crushed $HoMn_6Ge_6$ single crystals overlapped with

Rietveld refinement performed using the Fullprof software. The Rietveld refinement confirms that $HoMn_6Ge_6$ crystallizes into the hexagonal kagome $HfFe_6Ge_6$-type crystal structure with a space group of $P6/mmm$ (No. 191). The refined lattice parameters $a = b = 5.2415(5)$ $\AA$ and $c = 8.1831(4)$ $\AA$ confirm that the studied sample of $HoMn_6Ge_6$ is almost equivalent to the reported ones within the error-bars [33, 35]. Also, see Table I in the Supplemental Material [39] for a comparison of the structural parameters between our sample and the reported similar compounds in Refs. [33, 35]. The right-inset in Fig. 1(a) shows the XRD pattern taken on the flat surface of the single crystal, confirming that the crystal growth plane is parallel to (0001)-plane direction. Fig. 1(b) depicts the EDXS data conforming the exact chemical composition of the sample $Ho_{0.96}Mn_{5.74}Ge_6$. For convenience, hereafter, we represent it by the nominal composition of $HoMn_6Ge_6$. Since the crystals were grown out of Sn flux, the crystals were found with a maximum 2% of Sn impurity. The elemental mappings done for Ho, Mn, and Ge, as shown in the top insets of Fig. 1(b), imply a good homogeneity of the studied single crystals.

Longitudinal electrical resistivity [$\rho_{xx}(T)$] is plotted as a function of temperature, as shown in Fig. 2(a), measured without magnetic field (red-colored data) and with $\mu_0 H = 9$ T of magnetic field (blue-colored data) applied parallel to the z-axis [0001]. The low-temperature resistivity (< 100 K) can be reasonably fit with the quadratic equation of the Landau Fermi-liquid theory, $\rho_{xx}(T) = \rho_0 + \alpha T^2$. Here, $\rho_0 = 8.42$ $\mu\Omega cm$ is the residual resistivity due to impurity scattering and $\alpha = 2 \times 10^{-9}$ $\mu\Omega cm/K^2$ is the electron-electron scattering coefficient. Further, in the resistivity data ($\mu_0 H = 0$ T) we observe *kinks* at $T_1 \approx 270$ K and $T_2 \approx 215$. The transition temperatures T_1 and T_2 shift towards higher temperatures under the external magnetic fields. For instance, at a field of 9 T, the transition temperature T_2 shifted to 236 K, while we cannot identify T_1 under the 9 T field as the measurements were done only up to 300 K. This observation indicates the magnetic origin of the *kinks*. Further, the observation of T_1 and T_2 transition temperatures under zero field is consistent with a previous report on $HoMn_6Ge_6$ in which the temperature range between T_1 and T_2 is referred by a mixed magnetic state ($\widetilde{SS}$+AFM) [33]. Fig. 2(b) depicts the magnetoresistance percentage [$MR\% = (\rho_{xx}(T,H) - \rho_{xx}(T,0))/\rho_{xx}(T,0)$] plotted as a function of temperature from which another transition is identified at $T_3 \approx 35$ K, though it is not clearly visible from the $\rho_{xx}(T)$ data [see Fig. 2(a)]. Overall, the longitudinal electrical resistivity shows the metallic nature throughout the measured temperature range with a residual resistivity ratio (RRR) of $\rho_{xx}(300\text{K})/\rho_{xx}(2\text{K}) \approx 20$.

Fig. 2(c) presents the magnetization plotted as a function of temperature [$M(T)$] under the magnetic field $\mu_0 H = 0.05$ T applied parallel ($H \parallel z$) and perpendicular ($H \perp z$) to the z-axis, measured both in the field-cooled (FC) and zero-field-cooled (ZFC) modes. Clear

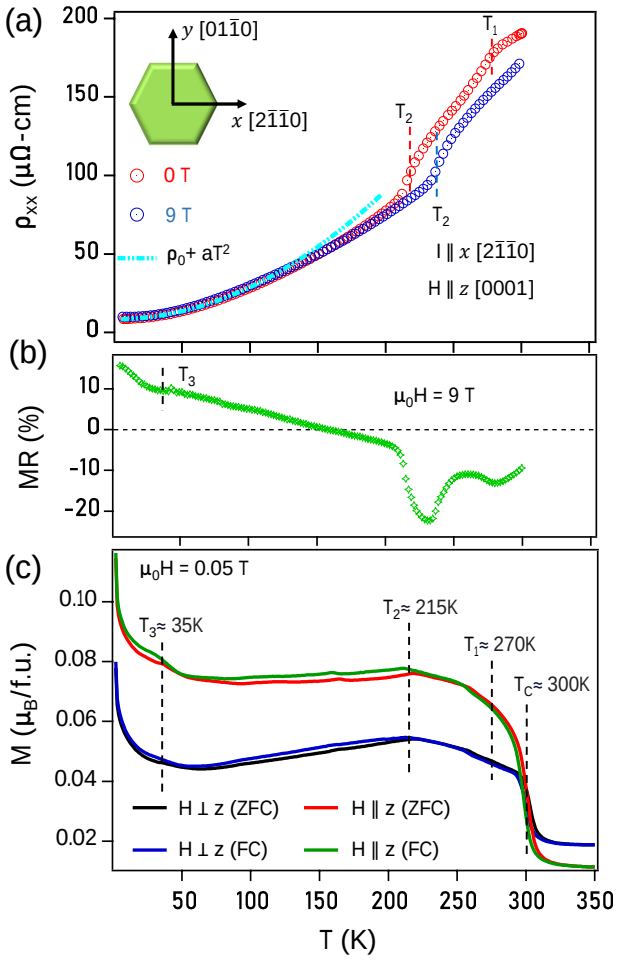

FIG. 2. (a) Longitudinal resistivity ρ_{xx} plotted as a function of temperature with current applied along x [2$\bar{1}\bar{1}$0]-axis for both 0 T (red curve) and 9 T (blue curve) fields applied along z [0001]-axis of the crystal. (b) Magnetoresistance MR(%)= $\frac{\rho_{xx}(9T)-\rho_{xx}(0T)}{\rho_{xx}(0T)} \times 100(\%)$ plotted as a function of temperature. (c) Magnetization plotted as a function of temperature [$M(T)$] for both $H \parallel z$ and $H \perp z$ directions measured under field-cooled and zero-field-cooled modes with $\mu_0 H = 0.05$ T.

overlapping between FC and ZFC data suggests that the magnetic moments are thermally reversible in the system throughout the measured temperature range of 2 - 350 K. On the other hand, previous neutron diffraction study on similar system revealed a complex magnetic structure with different magnetic states at different temperatures [35]. For instance, in the low-temperature region (< 55 K), the Ho and Mn magnetic moments form a skew spiral ($\widetilde{SS}$) structure, coupled antiferromagnetically, with a plane of moments making an angle θ_S with the z-axis [see Fig. 6(b)], producing finite net magnetization along both the in-plane and out-of-plane directions. Between 55 and 220 K, both wave vector (q) and phase angle (ϕ_S) increase monotonically with temperature. In the 220-260 K region, the $\widetilde{SS}$ structure gets distorted, ac-

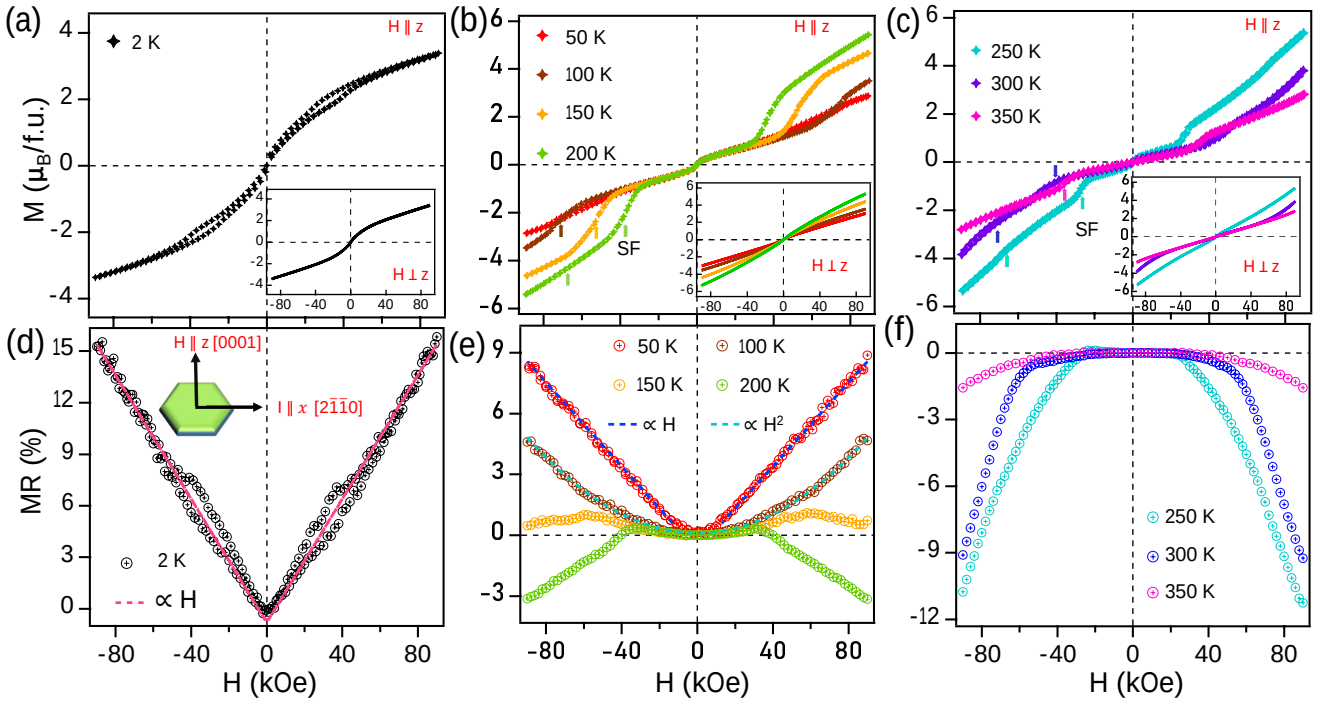

FIG. 3. (a),(b), and (c) Isothermal magnetization $M(H)$ measured at different temperatures for the fields applied parallel to the z-axis ($H \parallel z$). Insets in (a)-(c) show same for $H \perp z$. (d),(e), and (f) Field dependent magnetoresistance [MR(%)= $\frac{\rho_{xx}(H)-\rho_{xx}(0)}{\rho_{xx}(0)} \times 100(\%)$] measured for different temperatures.

companied by the Mn spin-reorientation, and thus eventually leading to a weak ferromagnetism at 300 K. Beyond 300 K the skew-spiral structure becomes a cycloid. In line with previous studies [33, 35, 40, 41] we also observe magnetic transitions in the magnetization data at $T_1 \approx 270$ K, $T_2 \approx 215$ K, and at $T_3 \approx 35$ K. Further, a weak ferromagnetic-like magnetization jump is noticed at $T_C \approx 300$ K. As can be seen from Fig. 2(c), the out-of-plane magnetization ($H \parallel z$) is significantly higher than the in-plane magnetization ($H \perp z$) below 300 K, while it is vice versa above 300 K. This observation hints at the fluctuating magnetic moments across the T_C. Also, note that a slight variation in the transition temperatures (T_1, T_2 and T_3) is noticed between our data and Refs. [33, 35], possibly due to different sample preparation methods. Specifically, the $M(T)$ of Ref. [33] shows a cusp at around 25 K and a rapid increase in $M(T)$ below 77 K, while no cusp is found but a rapid increase in $M(T)$ is found below 55 K in Ref. [35]. On the other hand, from our data we observe a cusp at 33 K and a rapid increase in $M(T)$ below 50 K [see Fig. 2(c)]. Similarly, the mixed magnetic state of AFM+$\widetilde{SS}$ is reported within the temperature range of 220-260 K in Ref. [35], 215-245 K in Ref. [33], while from our data we find it in a broader temperature range of 215-270 K..

Next, Figs. 3(a), 3(b), and 3(c) depict magnetization isotherms [$M(H)$] measured at different temperatures for $H \parallel z$ and $H \perp z$. We observe weak ferromagnetic-like $M(H)$ data when measured at 2 K for both $H \parallel z$ and $H \perp z$ at lower field regions without magnetization saturation. Further field-induced hysteresis is visible for $H \parallel z$ between 2 and 4 T but not for $H \perp z$, possibly due to the out-of-plane spin canting within this field range. This type of metamagnetic state is not observed at higher temperatures. Instead, an out-of-plane spin-flop transition has been found at a critical field (H_{SF}) that is temperature dependent, due to which a sudden increase in magnetization was noticed [see Figs. 3(b) and(c)]. However, the spin-flop transition is absent from the in-plane magnetization ($H \perp z$) at any measured temperature. A previous report also demonstrates similar spin-flop transitions in $HoMn_6Ge_6$ [33].

Isothermal magnetoresistance (MR) at different sample temperatures and with the fields applied parallel to the z-axis are shown in Figs. 3(d), 3(e), and 3(f). Fig. 3(d) demonstrates the MR measured at 2 K, where the MR is linearly dependent (red-dashed line) on the applied field in addition to the hysteresis between the fields 2 and 4 T that originated from the field-induced metamagnetic state [Fig. 3(a)]. From Fig. 3(e), we can see that the linear dependency of MR is intact up to 50 K. However, at 100 K, we observe a classical parabolic magnetoresistance. Though this parabolic nature is sustained at higher temperatures (150 and 200 K) as well, beyond the spin-flop (H_{SF}) transition, the MR starts to decrease with increasing the field for a given temperature.

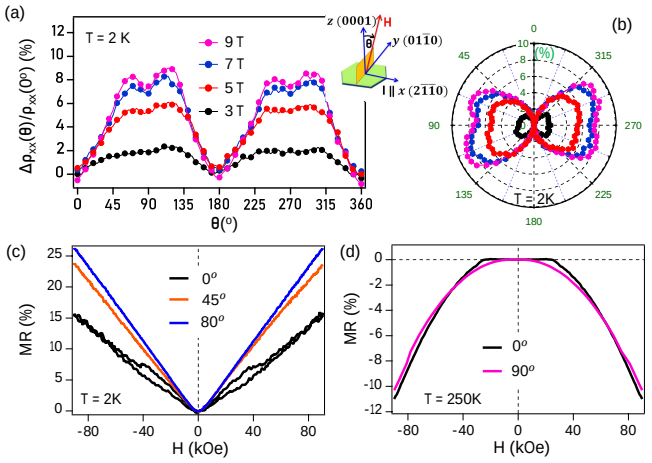

FIG. 4. (a) Angle dependent magnetoresistance [ADMR(%) $= \frac{\rho_{xx}(\theta)-\rho_{xx}(0^o)}{\rho_{xx}(0^o)} \times 100(\%)$] measured for various applied fields at 2 K. Inset in (a) is a schematic showing the ADMR measuring geometry. Here θ is the angle between z-axis and the applied field direction. (b) is same as (a) but plotted in polar coordinates for a better visualization. In (b) radius is the amplitude of ADMR(%). (c) Field dependent magnetoresistance (MR) measured at 2 K for different θ values. (d) is same as (c) but measured at 250 K of the sample temperature.

Eventually, beyond the H_{SF} the MR becomes negative above 150 K, consistent with the MR(T) data shown in Fig. 2(b) in which we can notice negative MR above 150 K when measured with 9 T. However, the MR becomes nearly field-independent as the temperature reaches 350 K.

Overall, $HoMn_6Ge_6$ shows a complex temperature dependent MR. Importantly, up to 50 K it shows a positive nonsaturating MR that is linearly depending on the applied field. There exist several mechanisms explaining the linear MR, such as (i) the presence of linear dispersive Dirac-like bands with very low effective mass near the Fermi level in the case of topological materials [42, 43], (ii) quasi-random resistor network model in the case of metal–semiconductor composites [44, 45], and (iii) carrier density fluctuations due to irregular current paths from the inhomogeneous or grain boundaries in the case of disordered systems [46, 47]. We can safely rule out the (ii) mechanism as our system is not a metal-semiconductor composite. Also, since our studied system is in the single crystalline form with no significant grain boundaries and with good homogeneity, we can rule out the mechanism (iii) also as the origin of linear MR. Previous reports on its sister compounds RMn_6Sn_6 suggested that the linear MR could originate from the Dirac-like linear bands [29]. In addition, previous band structure calculations on these systems showed several Dirac-like linear band dispersions crossing the Fermi level [36, 48]. To confirm that the linear MR originates from the linear Dirac-like topological band structure, we performed density functional theory (DFT) calculation, as discussed later explicitly.

Further, we measured the angle-dependent magnetoresistance (ADMR) with the current and field directions always kept perpendicular to each other such that only the field direction changes with the crystal axes as shown in the schematic of Fig. 4(a). The angle-dependent magnetoresistance is calculated as $\frac{\rho_{xx}(\theta)-\rho_{xx}(0^o)}{\rho_{xx}(0^o)}(\%)$ while the applied magnetic field is kept constant. As seen from Fig. 4(a), at 2 K, the MR is positive for all the applied magnetic fields but very sensitive to the field angle, suggesting a strong anisotropic MR in this system. Specifically, MR is minimum at the angles of 0°, 180°, and 360° and it is maximum at the angles 60°, 120°, 240°, and 300°. Also, the saddle points in the ADMR are observed at 90° and 270° for all the applied fields. For a better visualization, we plotted the ADMR in polar coordinates as shown in Fig. 4(b), from which we can clearly observe a butterfly pattern for the out-of-plane MR at 2 K. It is worth to mention here that the ADMR measured at 250 K is negligibly small (not shown) compared to the ADMR taken at 2 K. Next, Fig. 4(c) depicts the field-dependent MR plotted for different field angles (0°, 45°, and 80°) measured at 2 K, from which we observe linear MR at all field angles. Moreover, we see that the MR reaches almost 25% for $\theta = 80°$, and the hysteresis, which was present for $\theta = 0°$, has vanished at the other two angles. Fig. 4(d) depicts filed dependent MR taken at 0° and 90° filed angles, from which we observe the absence of spin-flop transition effect on the MR when measured at 90°, consistent with $M(H)$ for $H \perp z$.

Next, Fig. 5(a) demonstrate field-dependent Hall resistivity [$\rho_{xy}(H)$] measured at different sample temperatures. We see a deviation in the Hall resistivity, leading to an anomalous Hall effect, at the spin-flop transition temperature. Usually, in ferromagnets, the Hall resistivity can be expressed by $\rho_H = R_0\mu_0 H + R_S\mu_0 M$ [49], where R_0 is the ordinary Hall coefficient and R_S is the anomalous Hall coefficient. Although the anomalous Hall effect (AHE) mainly appears in ferromagnets, recently it has been widely observed in noncollinear antiferromagnets as well [17, 50–52]. From our Hall resistivity data, we can see that the anomalous Hall effect is induced by a spin-flop transition that resembles the $M(H)$ data shown in Figs. 3(a)-(c). Moreover, the above formula can be rewritten as $\frac{\rho_H}{\mu_0 H} = R_0 + R_S\frac{M}{H}$ which imitates a linear equation and intercept on the y-axis gives R_0 and slope gives the anomalous Hall coefficient R_S. Using this formalism, we have reasonably fitted the Hall resistivity as depicted in Fig. 5(a). The anomalous scaling factor (S_H) is calculated using the formula $S_H = \mu_0 R_S/\rho_{xx}^2$, where ρ_{xx} is the longitudinal resistivity. Fig. 5(c) depicts the normal Hall coefficient (R_0) plotted as a function of temperature. From Fig. 5(c), we further notice R_0 changing from positive to negative at around 215 K, which indicates hole-type (electron-type) carrier dominance below (above) 215 K.

As discussed above, a magnetic transition exists at around 215 K (T_2). It is possible that the change in magnetic structure influences the electronic structure near

the Fermi level and thus the switching of charge carrier type at 215 K. This observation suggests a strong correlation between the magnetic and electronic structures in these systems. Moreover, the value of R_S decreases rapidly with decreasing temperature and becomes negligibly small below 100 K. Whereas the S_H varies between 0.05 and 0.2 like in a typical ferromagnetic metal [49, 53]. Further from the relation $\mu_0 R_S = S_H \rho_{xx}^2$, it is clear that for very low resistivity ρ_{xx} values the contribution from AHE (R_S) is negligible so that only the ordinary Hall effect dominates at low temperatures. In Fig. 5(b), we have plotted the Hall conductivity as a function of temperature calculated using the formula, $\sigma_{xy} = -\frac{\rho_{xy}}{\rho_{xy}^2+\rho_{xx}^2}$. In Fig. 5(b), we have fitted the Hall conductivity curves using the single band model, $\sigma_{xy} = [\frac{n_h {\mu_h}^2}{1+(\mu_h B)^2}]eB$ as at low temperatures the hole carriers dominate the total Hall transport. Here, n_h is hole carrier density, and μ_h is hole mobility. From the fits, we derived the hole carrier concentration of n_h is 1.06×10^{20} cm^{-3} and hole mobility of $\mu = 0.049$ m^2/Vs at 2 K. These values are consistent with a previous report on these type of systems [29].

To uncover the mechanism of unsaturated linear MR, we performed density functional theory calculations as illustrated in Fig. 6. For the DFT calculations, we considered the magnetic structure as shown in Fig. 6(b), depicted by the neutron diffraction study on this system [35]. Fig. 6(c) displays the electronic band dispersion along the high-symmetry k-path of $\Gamma - M - K - \Gamma$ calculated without and with considering the spin-orbit coupling (SOC). We notice several linear band crossings (Dirac-like) from the electronic band structure at the K point near the Fermi level. One Dirac point (DP1) is observed at a binding energy of 90 meV below the Fermi level (E_F) that is gapless without SOC, but under SOC, the Dirac point is gapped by lifting the degeneracy. DP2 is found at a binding energy of 40 meV below the E_F, which is always gaped. DP3 is found at a binding energy of 250 meV above E_F, which is gapless for both with SOC and without SOC. Our calculations on $HoMn_6Ge_6$ align with previous calculations performed on $HoMn_6Sn_6$ [31, 36]. Particularly, the calculations on $HoMn_6Sn_6$ demonstrated that gap size at the Dirac points depends explicitly on the magnetic spin orientation with respect to the crystal axis [31, 36]. This means, larger (smaller) gaps were predicted for the fields applied along the out-of-plane (in-plane) direction. Since our calculations were performed with an angle of $\theta_S = 60°$ between the z-axis and plane of magnetic moments, which is neither out-of-plane nor in-plane, we observe both gapped and gapless Dirac points. This observation hints at the possibility of a critical angle of magnetic moments at which the Dirac states are gapless and robust under SOC.

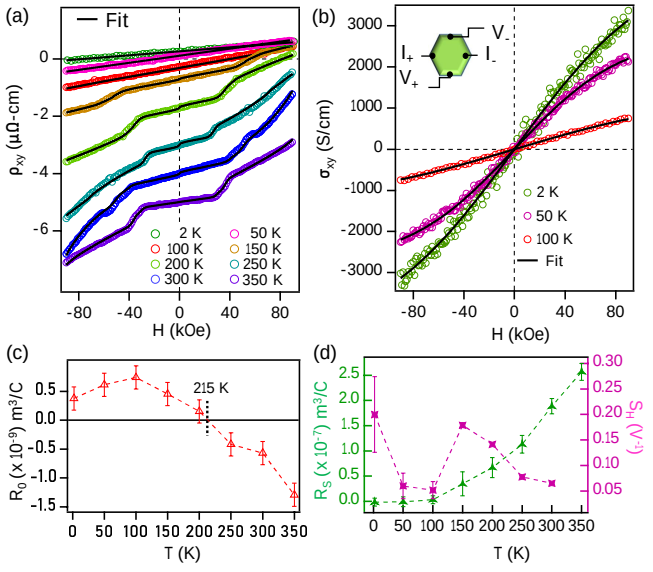

FIG. 5. (a) Field dependent Hall resistivity ρ_{xy} measured for different sample temperatures overlapped with the fits (black curves). (b) Field dependent Hall conductivity σ_{xy} plotted for 2, 50, and 100 K of sample temperatures. Inset in (b) schematically shows the Hall effect measuring geometry. (c) Normal Hall coefficient (R_0) plotted as a function of temperature. (d) Anomalous Hall coefficient (R_S) [left axis] and anomalous Hall scaling factor (S_H) [right axis] plotted as a function of temperature.

Apart from the linear band dispersions at the K point, we also observe two hole-like band dispersions (h_1 and h_2) crossing the Fermi level around K point and an electron-like (e_1) band dispersion crossing the Fermi level around the Γ point. No bands are found at the M-point crossing the Fermi level. In addition, we found several flat bands (fb_1, fb_2, and fb_3) that are dispersionless throughout the Brillouin zone. Figs. 6(d)-(f) show the three-dimensional view of the Fermi surface maps, which are mainly contributed by three types of Fermi pockets; one of them is the electron-like (e_1) pocket with an almost cylindrical shape as shown in Fig. 6(d), the second one is the hole-like (h_1) pocket, which is close to one-third of a cylinder shared by each corner of the hexagon, as shown in Fig. 6(e), and the last one is the hip-roof-shaped hole-like (h_2) pocket at the K point. With the help of these three types of Fermi pockets, we estimated the hole carrier density n_h=5.3×10^{20}/cm^3 and electron carrier density n_e=3.6×10^{20}/cm^3 to find the net hole carrier density of 1.7×10^{20}/cm^3 using Luttinger's theorem [54] [see Supplemental Material [39]]. Interestingly, this value is close to the experimentally calculated net carrier density (1.06×10^{20} cm^{-3}) from the Hall data at 2 K. The estimated hole and electron carrier densities are nearly equal, suggesting a possible charge compensation in this system [55, 56]. Further, the estimated net carrier density of 1.06×10^{20} cm^{-3} suggests $HoMn_6Ge_6$ to be a semimetal [57, 58]. Figs. 6(g) and 6(h) illustrate the Fermi surfaces projected onto the $k_x - k_y$ and $k_x - k_z$ planes, clearly showing the electron-like Fermi pocket at the Γ and hole-like Fermi pockets at the K point.

As for the angle-dependent magnetoresistance

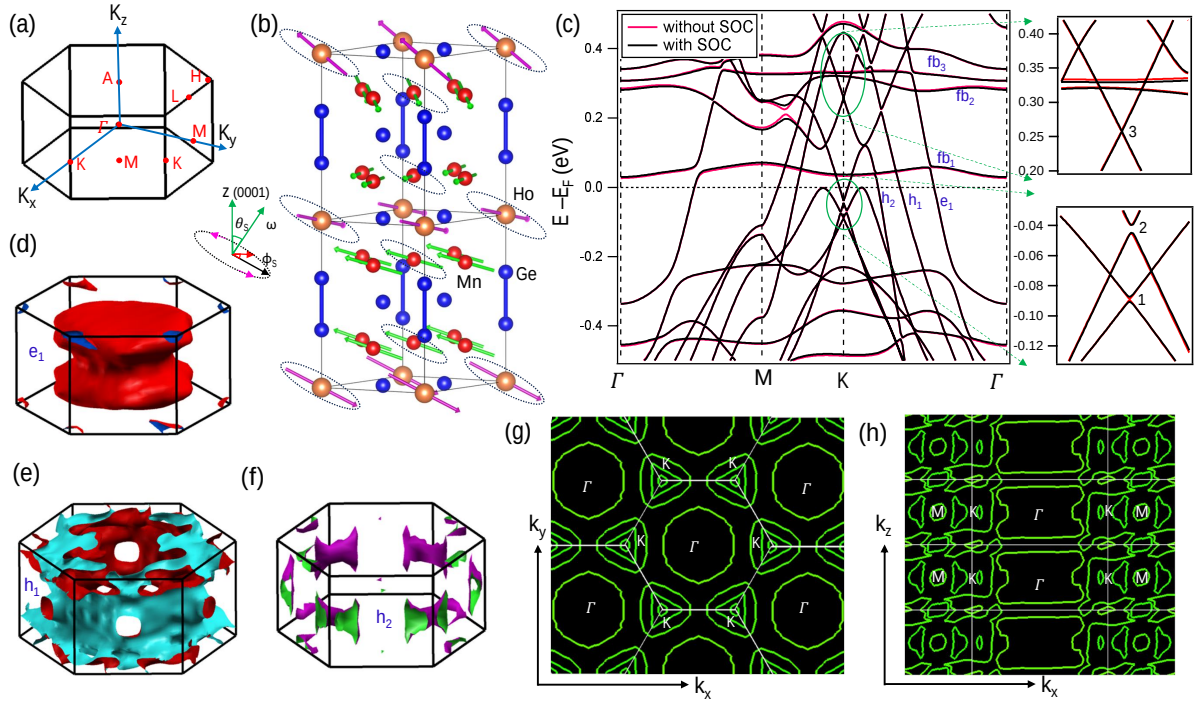

FIG. 6. (a) Hexagonal Brillouin zone showing the positions of various high symmetry points. (b) Low temperature skew-spiral ($\widetilde{SS}$) magnetic structure of $HoMn_6Ge_6$ [35]. Here, $\theta_s = 60^o$ and $\phi_s = 71.2^o$. (c) Electronic band structure of $HoMn_6Ge_6$ calculated for the magnetic configuration shown in (b) with (black-colored) and without (red-colored) including the spin-orbit coupling (SOC). The right-side panels of (c) show the zoomed-in band structure to clearly see various Dirac points. (d), (e), and (f) show the calculated Fermi surface maps in three-dimensional. (g) and (h) show the constant energy contours taken at the Fermi level in the $k_x - k_y$ and $k_x - k_z$ momentum planes, respectively.

(ADMR) measurements, the magnetic field is always perpendicular to the current direction, which does not change the Lorentz force acting on the charge carriers. The spin-charge scattering can be neglected at low temperatures as the mean free path of the charge carriers is much higher in this system at 2 K ($\approx 0.67\ \mu m$) compared to the distance of $Mn - Mn$ (2.62 Å) or $Ho - Ho$ (5.24 Å) magnetic moments. This leads us to conclude that the anisotropic ADMR has an electronic band structure origin rather than a magnetism origin. The Fermi velocity can be calculated as $v_k = \frac{1}{\hbar}\nabla_k \epsilon_k$, which depends on the local curvature of the Fermi surface cross-section. The smaller the orbit of the Fermi surface cross-section, the greater the local curvature, leading to a higher Fermi velocity. Hence, a high microscopic Lorentz force would act on the charge carriers [59–61]. Our calculations indicate that the electron pocket e_1 and hole pocket h_1 exhibit nearly cylindrical shapes, with their diameters and heights being quite similar in value, making them nearly isotropic. Only the h_2 hole pocket has an anisotropic shape (hip-roof-shaped), which could be the possible origin of this high anisotropic ADMR. Because when the field is applied along the z-axis, the charge carriers are subjected to orbit on the $k_x - k_y$ plane. Similarly, for the fields applied along the y-axis the carriers would orbit on the $k_x - k_z$ plane. As observed in Fig. 6(g), the Fermi sheets at K point are nearly circular for $H \parallel z$ [see Fig. 4(a) for $\theta = 0^o$]. Only the out-of-plane Fermi sheets ($k_x - k_z$) have substantial curvature [see Fig. 6(h)] which are detected experimentally for $H \parallel y$ [see Fig. 4(a) for $\theta = 90^o$]. Therefore, we think the asymmetric MR originated from the asymmetric out-of-plane Fermi pockets. Further, as evidenced by our DFT band structure calculations, the linear nonsaturating MR is mainly contributed by the linear Dirac-like bands near the Fermi level.

IV. SUMMARY

In summary, using the Sn flux, we have grown high-quality single crystals of $HoMn_6Ge_6$. Electrical resistivity, with a few magnetic transition-driven anomalies, demonstrates an overall metallic nature throughout the measured temperature range. A crossover from negative to positive magnetoresistance (MR) is observed at a critical temperature of 150 K. While the Dirac-like linear band dispersions mainly drive the linear nonsaturating positive MR exits in the low-temperature region, the negative MR observed in the higher temperature region is due to the spin-flop type magnetic transition. We found an anomalous Hall effect in addition to a dominant charge

carrier switching across 215 K. We performed electronic band structure calculations on $HoMn_6Ge_6$ by considering the skew-spiral magnetic structure of the system to realize large anisotropy in the out-of-plane Fermi sheets. We suggest that the large anisotropic out-of-plane magnetoresistance observed in $HoMn_6Ge_6$ originated from the anisotropic out-of-plane Fermi surfaces. The band structure calculations predict several Dirac-type band crossings at the K point near the Fermi level.

ACKNOWLEDGMENTS

This research has used the Technical Research Centre (TRC) Instrument Facilities of S. N. Bose National Centre for Basic Sciences, established under the TRC project of the Department of Science and Technology, Govt. of India.

[1] M. S. S. Brooks, L. Nordström, and B. Johansson, Rare-earth transition-metal intermetallics, Physica B **172**, 95 (1991).
[2] F. D. M. Haldane, Model for a Quantum Hall Effect without Landau Levels: Condensed-Matter Realization of the "Parity Anomaly", Phys. Rev. Lett. **61**, 2015 (1988).
[3] C. Z. Chang, J. Zhang, X. Feng, J. Shen, Z. Zhang, M. Guo, K. Li, Y. Ou, P. Wei, L. L. Wang, Z. Q. Ji, Y. Feng, S.-H. Ji, X. Chen, J.-F. Jia, X. Dai, Z. Fang, S. C. Zhang, K. He, Y. Wang, L. Lu, X. Cun, and Q. K. Xue, Experimental observation of the quantum anomalous Hall effect in a magnetic topological insulator, Science **340**, 167 (2013).
[4] B. Keimer and J. E. Moore, The physics of quantum materials, Nat. Phys. **13**, 1045 (2017).
[5] S. Sachdev, Topological order, emergent gauge fields, and Fermi surface reconstruction, Rep. Prog. Phys. **82**, 014001 (2018).
[6] Y. Tokura, K. Yasuda, and A. Tsukazaki, Magnetic topological insulators, Nature Reviews Physics **1**, 126 (2019).
[7] P. C. Canfield, New materials physics, Rep. Prog. Phys. **83**, 016501 (2019).
[8] A. Hirohata, K. Yamada, Y. Nakatani, I. L. Prejbeanu, B. Dieny, P. Pirro, and B. Hillebrands, Review on spintronics: Principles and device applications, J. Magn. Magn. Mater. **509**, 166711 (2020).
[9] A. Kitaev, Anyons in an exactly solved model and beyond, Ann. Phys. **321**, 2 (2006).
[10] J. S. Helton, K. Matan, M. P. Shores, E. A. Nytko, B. M. Bartlett, Y. Yoshida, Y. Takano, A. V. Suslov, Y. Qiu, J. Chung, D. G. Nocera, and Y. S. Lee, Spin Dynamics of the Spin-1/2 Kagome Lattice Antiferromagnet $ZnCu_3(OH)_6Cl_2$ Spin Dynamics of the Spin-1/2 Kagome Lattice Antiferromagnet $ZnCu_3(OH)_6Cl_2$, Phys. Rev. Lett. **98**, 107204 (2007).
[11] T. Han, J. S. Helton, S. Chu, D. G. Nocera, J. A. Rodriguez-Rivera, C. Broholm, and Y. S. Lee, Fractionalized excitations in the spin-liquid state of a kagome-lattice antiferromagnet, Nature **492**, 406 (2012).
[12] Y. Kasahara, T. Ohnishi, Y. Mizukami, O. Tanaka, S. Ma, K. Sugii, N. Kurita, H. Tanaka, J. Nasu, Y. Motome, T. Shibauchi, and Y. Matsuda, Majorana quantization and half-integer thermal quantum Hall effect in a Kitaev spin liquid, Nature **559**, 227 (2018).
[13] B. Sutherland, Localization of electronic wave functions due to local topology, Phys. Rev. B **34**, 5208 (1986).
[14] D. Leykam, A. Andreanov, and S. Flach, Artificial flat band systems: from lattice models to experiments, Advances in Physics: X **3**, 1473052 (2018).
[15] M. Kang, L. Ye, S. Fang, J.-S. You, A. Levitan, M. Han, J. I. Facio, C. Jozwiak, A. Bostwick, E. Rotenberg, M. Chan, R. McDonald, D. Graf, K. Kaznatcheev, E. Vescovo, D. C. Bell, E. Kaxiras, J. Van Den Brink, M. Richter, M. P. Ghimire, J. Checkelsky, and R. Comin, Dirac fermions and flat bands in the ideal kagome metal FeSn, Nat. Mater. **19**, 163 (2019).
[16] M. Kang, S. Fang, L. Ye, H. C. Po, J. D. Denlinger, C. Jozwiak, A. Bostwick, E. Rotenberg, E. Kaxiras, J. Checkelsky, and R. Comin, Topological flat bands in frustrated kagome lattice CoSn, Nat. Commun. **11**, 4004 (2020).
[17] S. Nakatsuji, N. Kiyohara, and T. Higo, Large anomalous Hall effect in a non-collinear antiferromagnet at room temperature, Nature **527**, 212 (2015).
[18] K. Kuroda, T. Tomita, M. T. Suzuki, C. Bareille, A. A. Nugroho, P. Goswami, M. Ochi, M. Ikhlas, M. Nakayama, S. Akebi, R. Noguchi, R. Ishii, N. Inami, K. Ono, H. Kumigashira, A. Varykhalov, T. Matsuki, T. Koretsune, R. Arita, S. Shin, T. Kondo, and S. Nakatsuji, Evidence for magnetic Weyl fermions in a correlated metal, Nat. Mater. **16**, 1090 (2017).
[19] E. Liu, Y. Sun, N. Kumar, L. Muechler, A. Sun, L. Jiao, S. Yang, D. Liu, A. Liang, Q. Xu, J. Kroder, V. Süß, H. Borrmann, C. Shekhar, Z. Wang, C. Xi, W. Wang, W. Schnelle, S. Wirth, Y. Chen, S. T. B. Goennenwein, and C. Felser, Giant anomalous Hall effect in a ferromagnetic kagome-lattice semimetal, Nat. Phys. **14**, 1125 (2018).
[20] L. Ye, M. Kang, J. Liu, F. Von Cube, C. Wicker, T. Suzuki, C. Jozwiak, A. Bostwick, E. Rotenberg, D. C. Bell, L. Fu, R. Comin, and J. Checkelsky, Massive Dirac fermions in a ferromagnetic kagome metal, Nature **555**, 638 (2018).
[21] D. F. Liu, A. Liang, E. K. Liu, Q. Xu, Y. W. Li, C. Chen, D. Pei, W. Shi, S.-k. Mo, P. Dudin, T. K. Kim, C. Cacho, G. Li, Y. Sun, L. Yang, Z. K. Liu, S. S. P. Parkin, C. Felser, and Y. L. Chen, Magnetic Weyl semimetal phase in a Kagomé crystal, Science **365**, 1282 (2019).
[22] G. Xu, B. Lian, and S.-C. Zhang, Intrinsic Quantum Anomalous Hall Effect in the Kagome Lattice $Cs_2LiMn_3F_{12}$, Phys. Rev. Lett. **115**, 186802 (2015).
[23] J.-X. Yin, W. Ma, T. A. Cochran, X. Xu, S. S. Zhang, H.-J. Tien, N. Shumiya, G. Cheng, K. Jiang, B. Lian, Z. Song, G. Chang, I. Belopolski, D. Multer, M. Litskevich, Z. J. Cheng, X. Yang, B. Swidler, H. Zhou, H. Lin, T. Neupert, Z. Wang, N. Yao, T. R. Chang, S. Jia, and M. Z. Hasan, Quantum-limit Chern topological magnetism in $TbMn_6Sn_6$, Nature **583**, 533 (2020).

[24] M. Hirschberger, T. Nakajima, S. Gao, L. Peng, A. Kikkawa, T. Kurumaji, M. Kriener, Y. Yamasaki, H. Sagayama, H. Nakao, K. Ohishi, K. Kakurai, Y. Taguchi, X. Yu, T.-H. Arima, and Y. Tokura, Skyrmion phase and competing magnetic orders on a breathing kagomé lattice, Nature Communications **10** (2019).

[25] D. Chakrabartty, S. Jamaluddin, S. K. Manna, and A. K. Nayak, Tunable room temperature magnetic skyrmions in centrosymmetric kagome magnet Mn_4Ga_2Sn, Communications physics **5** (2022).

[26] T. Chen, T. Tomita, S. Minami, M. Fu, T. Koretsune, M. Kitatani, M. Ikhlas, D. Nishio-Hamane, R. Ishii, F. Ishii, R. Arita, and S. Nakatsuji, Anomalous transport due to Weyl fermions in the chiral antiferromagnets Mn_3X, X = Sn, Ge, Nature Communications **12** (2021).

[27] T. Chen, S. Minami, A. Sakai, Y. Wang, Z. Feng, T. Nomoto, M. Hirayama, R. Ishii, T. Koretsune, R. Arita, and S. Nakatsuji, Large anomalous Nernst effect and nodal plane in an iron-based kagome ferromagnet, Sci. Adv. **8**, eabk1480 (2022).

[28] Z. Hou, W. Ren, B. Ding, G. Xu, Y. Wang, B. Yang, Q. Zhang, Y. Zhang, E. Liu, F. Xu, W. Wang, G. Wu, X. Zhang, B.-G. Shen, and Z. Zhang, Observation of Various and Spontaneous Magnetic Skyrmionic Bubbles at Room Temperature in a Frustrated Kagome Magnet with Uniaxial Magnetic Anisotropy, Adv. Mater. **29**, 1701144 (2017).

[29] W. Ma, X. Xu, J.-X. Yin, H. Yang, H. Zhou, Z.-J. Cheng, Y. Huang, Z. Qu, F. Wang, M. Z. Hasan, and S. Jia, Rare Earth Engineering in $R\mathrm{Mn_6Sn_6}$ (R = Gd−Tm, Lu) Topological Kagome Magnets, Phys. Rev. Lett. **126**, 246602 (2021).

[30] L. Gao, S. Shen, Q. Wang, W. Shi, Y. Zhao, C. Li, W. Cao, C. Pei, J.-Y. Ge, G. Li, J. Li, Y. Chen, S. Yan, and Y. Qi, Anomalous Hall effect in ferrimagnetic metal $\mathrm{RMn_6Sn_6}$ (R = Tb, Dy, Ho) with clean Mn kagome lattice, Appl. Phys. Lett. **119**, 092405 (2021).

[31] F. Kabir, R. Filippone, G. Dhakal, Y. Lee, N. Poudel, J. Casey, A. P. Sakhya, S. Regmi, R. Smith, P. Manfrinetti, L. Ke, K. Gofryk, M. Neupane, and A. K. Pathak, Unusual magnetic and transport properties in $\mathrm{HoMn_6Sn_6}$ kagome magnet, Phys. Rev. Mater. **6**, 064404 (2022).

[32] D. Campbell, J. Collini, J. Sławińska, C. Autieri, L. Wang, K. Wang, B. Wilfong, Y. S. Eo, P. M. Neves, D. Graf, E. E. Rodriguez, N. P. Butch, M. B. Nardelli, and J. Paglione, Topologically driven linear magnetoresistance in helimagnetic FeP, npj quantum materials **6** (2021).

[33] H. Zhou, M. Shi, Y. Huang, W. Ma, X. Xu, J. Wang, and S. Jia, Metamagnetic transition and anomalous Hall effect in Mn-based kagomé magnets $R\mathrm{Mn_6Ge_6}$(R = Tb−Lu), Phys. Rev. Mater. **7**, 024404 (2023).

[34] G. Venturini, R. Welter, and B. Malaman, Crystallographic data and magnetic properties of $\mathrm{RT_6Ge_6}$ compounds (R Sc, Y, Nd, Sm, Gd Lu; T Mn, Fe), Journal of Alloys and Compounds **185**, 99 (1992).

[35] P. Schobinger-Papamanteilos, A neutron diffraction study of the magnetic ordering of $\mathrm{HoMn_6Ge_6}$, J. Magn. Magn. Mater. **139**, 119 (1995).

[36] Y. Lee, R. Skomski, X. Wang, P. P. Orth, Y. Ren, B. Kang, A. K. Pathak, A. Kutepov, B. N. Harmon, R. J. McQueeney, I. I. Mazin, and L. Ke, Interplay between magnetism and band topology in the kagome magnets $R\mathrm{Mn_6Sn_6}$, Phys. Rev. B **108**, 045132 (2023).

[37] J. P. Perdew, K. Burke, and M. Ernzerhof, Generalized Gradient Approximation Made Simple, Phys. Rev. Lett. **77**, 3865 (1996).

[38] P. Giannozzi, S. Baroni, N. Bonini, M. Calandra, R. Car, C. Cavazzoni, D. Ceresoli, G. L. Chiarotti, M. Cococcioni, I. Dabo, *et al.*, QUANTUM ESPRESSO: a modular and open-source software project for quantum simulations of materials, J. Phys.: Condens. Matter **21**, 395502 (2009).

[39] See Supplemental Material at [URL will be inserted by publisher] for additional structural informaiton.

[40] G. Venturini, A. Vernière, and B. Malaman, Multi spin-reorientation process in $\mathrm{HfFe_6Ge_6}$-type $\mathrm{HoMn_6Ge_{6-x}Ga_x}$ compounds (x=0.2, 0.4, 1.0), Journal of Alloys and Compounds **320**, 46 (2001).

[41] A. Mar, C. Lefèvre, and G. Venturini, Anisotropic transport properties measured in $\mathrm{HoMn_6Ge_6}$ single crystals, Journal of Magnetism and Magnetic Materials **269**, 380 (2004).

[42] A. A. Abrikosov, Quantum magnetoresistance, Phys. Rev. B **58**, 2788 (1998).

[43] A. A. Abrikosov, Quantum linear magnetoresistance, EPL **49**, 789 (2000).

[44] J.-P. Xu, Z. Duan-Ming, Z. Deng, Y. Fu, Z. Li, and Y. Pan, Quasi-Random resistor network model for linear magnetoresistance of Metal–Semiconductor composite, Chin. Phys. Lett. **25**, 4124 (2008).

[45] N. Ramakrishnan, Y. T. Lai, S. Lara, M. M. Parish, and S. Adam, Equivalence of effective medium and random resistor network models for disorder-induced unsaturating linear magnetoresistance, Phys. Rev. B **96**, 224203 (2017).

[46] R. Xu, A. Husmann, T. F. Rosenbaum, M.-L. Saboungi, J. E. Enderby, and P. B. Littlewood, Large magnetoresistance in non-magnetic silver chalcogenides, Nature **390**, 57 (1997).

[47] M. M. Parish and P. B. Littlewood, Non-saturating magnetoresistance in heavily disordered semiconductors, Nature **426**, 162 (2003).

[48] G. Dhakal, F. Cheenicode Kabeer, A. K. Pathak, F. Kabir, N. Poudel, R. Filippone, J. Casey, A. Pradhan Sakhya, S. Regmi, C. Sims, K. Dimitri, P. Manfrinetti, K. Gofryk, P. M. Oppeneer, and M. Neupane, Anisotropically large anomalous and topological Hall effect in a kagome magnet, Phys. Rev. B **104**, L161115 (2021).

[49] N. Nagaosa, J. Sinova, S. Onoda, A. H. MacDonald, and N. P. Ong, Anomalous Hall effect, Rev. Mod. Phys. **82**, 1539 (2010).

[50] Y. Luo, F. Ronning, N. Wakeham, X. Lu, T. Park, Z.-A. Xu, and J. D. Thompson, Pressure-tuned quantum criticality in the antiferromagnetic Kondo semimetal $\mathrm{CeNi_{2-\delta}As_2}$, Proc. Natl. Acad. Sci. U. S. A. **112**, 13520 (2015).

[51] T. Suzuki, R. Chisnell, A. Devarakonda, Y.-t. Liu, F. Wang, D. Xiao, J. W. Lynn, and J. Checkelsky, Large anomalous Hall effect in a half-Heusler antiferromagnet, Nat. Phys. **12**, 1119 (2016).

[52] J. Niu, B. Yan, Q. Ji, Z. Liu, M. Li, P. Gao, Y. Zhang, D. Yu, and X. Wu, Anomalous Hall effect and magnetic orderings in nanothick V_5S_8, Phys. Rev. B **96**, 075402 (2017).

[53] Q. Wang, S. Sun, X. Zhang, F. Pang, and H. Lei, Anomalous Hall effect in a ferromagnetic Fe_3Sn_2 single crystal with a geometrically frustrated Fe bilayer kagome lattice, Phys. Rev. B **94**, 075135 (2016).

[54] J. M. Luttinger, Fermi Surface and Some Simple Equilibrium Properties of a System of Interacting Fermions, Phys. Rev. **119**, 1153 (1960).

[55] M. N. Ali, J. Xiong, S. Flynn, J. Tao, Q. Gibson, L. M. Schoop, T. Liang, N. Haldolaarachchige, M. Hirschberger, N. P. Ong, and R. J. Cava, Large, non-saturating magnetoresistance in WTe_2, Nature **514**, 205 (2014).

[56] S. Thirupathaiah, R. Jha, B. Pal, J. S. Matias, P. K. Das, I. Vobornik, R. A. Ribeiro, and D. D. Sarma, Temperature-independent band structure of WTe_2 as observed from angle-resolved photoemission spectroscopy, Phys. Rev. B **96**, 165149 (2017).

[57] Y. Qi, P. G. Naumov, M. N. Ali, C. R. Rajamathi, W. Schnelle, O. I. Barkalov, M. Hanfland, S. C. Wu, C. Shekhar, Y. Sun, V. Süß, M. Schmidt, U. Schwarz, E. Pippel, P. Werner, R. Hillebrand, T. Förster, E. Kampert, S. S. P. Parkin, R. J. Cava, C. Felser, B. Yan, and S. A. Medvedev, Superconductivity in Weyl semimetal candidate $MoTe_2$, Nat. Commun. **7**, 11038 (2016).

[58] S. Thirupathaiah, R. Jha, B. Pal, J. S. Matias, P. K. Das, P. K. Sivakumar, I. Vobornik, N. C. Plumb, M. Shi, R. A. Ribeiro, and D. D. Sarma, $MoTe_2$: An uncompensated semimetal with extremely large magnetoresistance, Phys. Rev. B **95**, 241105 (2017).

[59] A. Collaudin, B. Fauqué, Y. Fuseya, W. Kang, and K. Behnia, Angle Dependence of the Orbital Magnetoresistance in Bismuth, Phys. Rev. X **5**, 021022 (2015).

[60] J. Wang, H. Yang, L. Ding, W. You, C. Xi, J. Cheng, Z. Shi, C. Cao, Y. Luo, Z. Zhu, J. Dai, M. Tian, and Y. Li, Angle-dependent magnetoresistance and its implications for Lifshitz transition in W_2As_3, npj Quantum Materials **4**, 58 (2019).

[61] S. Zhang, Q. Wu, Y. Liu, and O. V. Yazyev, Magnetoresistance from Fermi surface topology, Phys. Rev. B **99**, 035142 (2019).